NeuroImage 305 (2025) 120979

Contents lists available at ScienceDirect

NeuroImage

journal homepage: www.elsevier.com/locate/ynimg

Resolution dependence of vessel size index across various brain regions

DongKyu Lee [a,b], Yelim Gong [a,c], Abel Worku Tessema [a], SoHyun Han [d,*], Hyung Joon Cho [a,**]

[a] Department of Biomedical Engineering, Ulsan National Institute of Science and Technology, Ulsan, Republic of Korea
[b] Brain Tech Center, Korea Brain Research Institute, Daegu, Republic of Korea
[c] Department of Medical Information, Chung-Ang University Gwangmyeong Hospital, Gyeonggi-do, Republic of Korea
[d] Center for Bio-imaging and Translational Research, Korea Basic Science Institute, Cheongju, Republic of Korea

ARTICLE INFO

Keywords:
Vessel size imaging
Vessel size index
Partial volume averaging
Resolution dependence

ABSTRACT

Magnetic resonance imaging (MRI) excels at detecting quantitative changes in microvascular parameters such as cerebral blood volume, cerebral blood flow, and vessel size index (VSI), which are essential for diagnosing and monitoring cerebrovascular diseases. Absolute VSI estimation, often utilizing superparamagnetic iron oxide nanoparticles as contrast agents, relies on measuring transverse relaxation rates (ΔR_2^* and ΔR_2). This study systematically investigates the spatial resolution dependence of VSI using Monte Carlo simulations and in vivo rat brain MRI experiments. Monte Carlo simulations modeled randomly oriented vasculatures with various vessel sizes, revealing that ΔR_2 values are significantly higher at an in-plane spatial resolution of 125 × 125 μm² compared to lower resolutions, particularly for smaller vessels. In vivo experiments on 13 rats using a 7 T MRI scanner compared VSI measurements at spatial resolutions of 125 μm² and 250 μm² across different brain regions. Results indicated region-specific VSI variations, with smaller vessels showing more pronounced resolution-dependent changes. The corpus callosum and hippocampal formation regions in particular exhibited significant increases in VSI at lower resolutions. The observed variability is attributed to the differing sensitivities of ΔR_2^* and ΔR_2 to vessel size. Corroboration between the experimental data and simulation findings emphasizes the necessity of optimizing spatial resolution to ensure accurate VSI quantification and enhance the precision of neuro-microvascular imaging techniques.

1. Introduction

Magnetic resonance imaging (MRI) gives access to detect microvascular variations such as in cerebral blood volume, cerebral blood flow, and microvascular architecture, which play an important role in the diagnosis and monitoring therapeutic responses of cerebrovascular diseases. (Jahng et al., 2014) Among such variations, microvascular architectural information such as vessel size index (VSI) has emerged as a potentially useful biomarker for monitoring microvasculature changes in response to therapies. (Tropres et al., 2001; Kiselev et al., 2005) VSI techniques are designed to assess microvessels smaller than the imaging voxel size that cannot be directly measured with conventional MRI. VSI can be estimated by measuring changes in transverse relaxation rates, i.e., ΔR_2^* and ΔR_2, from gradient and spin echoes induced by the injection of a contrast agent (CA) into the bloodstream. (Tropres et al., 2001) As one of various CAs, superparamagnetic iron oxide nanoparticles (SPIONs) are often used to estimate VSI by taking advantage of a long blood half-life, which allows for extended imaging time and potentially improved contrast-to-noise ratio in VSI measurements. (Pankhurst et al., 2003)

The inception of VSI techniques involved correlating the unique dependencies of changes in gradient echo and spin echo transverse relaxation rates (ΔR_2^* and ΔR_2, respectively) with the size of paramagnetic blood vessels. (Yablonskiy and Haacke, 1994; Kiselev and Posse, 1998; Kiselev and Posse, 1999; Dennie et al., 1998; Jensen and Chandra, 2000) Numerical simulations have indicated that ΔR_2^* shows sensitivity to a broad range of vessel sizes, increasing with microvessel radius before reaching a somewhat plateau for larger vessels. In contrast, ΔR_2 is capillary-weighted (radius < 10 μm), exhibiting a bell-shaped curve since spin echo minimizes the macroscopic magnetic susceptibility effect of large vessels due to the 180° refocusing pulse. (Boxerman et al., 1995) Increasing the magnetic field strength and

* Corresponding author at: Korea Basic Science Institute, Cheongju, Republic of Korea.
** Corresponding author at: 105-222, 50 UNIST-gil, Eonyang-eup, Ulju-gun, Ulsan, Republic of Korea.
E-mail addresses: hansomain256@kbsi.re.kr (S. Han), hjcho@unist.ac.kr (H.J. Cho).

https://doi.org/10.1016/j.neuroimage.2024.120979
Received 31 August 2024; Received in revised form 25 November 2024; Accepted 16 December 2024
Available online 17 December 2024

concentration of CAs enhances the values of ΔR_2^* and ΔR_2 for small radii blood vessels, which is expected to further increase capillary sensitivity in VSI. Expanding on the idea that the dimensionless ratio $\Delta R_2^*/\Delta R_2$ increases proportionally with vessel diameter, VSI (expressed in units of μm) was introduced as a quantitative measure to evaluate the average vessel radius within a voxel. (Tropres et al., 2001; Kiselev et al., 2005) Quantification of VSI requires consideration of additional factors including the water diffusion rate, absolute blood volume fraction (BVf), and CA concentration. With a focus on these parameters, several studies have been conducted to improve VSI quantification to enhance precision, reliability, and clinical applicability. (Kiselev et al., 2005; Emblem et al., 2013; Troprès et al., 2015; Chakhoyan et al., 2019)

To effectively accommodate specific experimental conditions such as limited scan times, required SNR values, and spatial resolutions to maintain structural differentiation, (Matsuda et al., 2003; Chappell et al., 2021) it is important to determine a reasonable spatial resolution for VSI. In general, VSI research has explored a wide range of spatial resolutions, (Bosomtwi et al., 2008; Lin et al., 2008; Serduc et al., 2008; Valable et al., 2008; Lu et al., 2009; Weidensteiner et al., 2009; Bouchet et al., 2010; Farrar et al., 2011; Lemasson et al., 2011; Coquery et al., 2012; Moisan et al., 2012; Boehm-Sturm et al., 2013) typically between 100 and 500 μm^2 in-plane resolution for preclinical studies. Ensuring consistent ΔR_2^* and ΔR_2 values across various spatial resolutions is crucial for maintaining the reliability of VSI measurements, especially at lower spatial resolutions due to partial volume effects. Specifically, the impact of the imaging voxel size can vary between spin and gradient echo acquisitions within the same region of interest. (Rossi et al., 2013; Lee et al., 2018; Meloche et al., 2022) This discrepancy arises from the fact that molecular diffusion near paramagnetic blood vessels predominantly influences ΔR_2, while static dephasing significantly affects ΔR_2^*. However, the impact of spatial resolution on ΔR_2^*, ΔR_2, and VSI has not undergone systematic investigation, to the best of our knowledge.

In this study, Monte Carlo (MC) simulations were performed to investigate the spatial resolution dependence of ΔR_2^*, ΔR_2, and VSI by generating randomly oriented vasculatures with various vessel sizes. Additionally, we examined the spatial resolution dependence of in vivo VSI in rat brains, focusing on commonly used spatial resolutions of 125 μm^2 and 250 μm^2 in rodent studies. Specifically, we compared the spatial resolution–dependent VSI in various brain regions including the cortex, corpus callosum, striatum, hippocampal formation, thalamus, macrovessel area, and ventricles. Our comprehensive investigation shows how the spatial resolution heterogeneously affects VSI in various brain regions due to the different tendencies of ΔR_2^* and ΔR_2 values with respect to vessel radii.

2. Methods

2.1. Animal models

Animal experiments were performed in accordance with the Animal Protection Act of Korea under the guidelines and regulations approved by the Institutional Animal Care and Use Committee of the Ulsan National Institute of Science and Technology. All experiments were reported in compliance with the ARRIVE guidelines (Animal Research: Reporting In Vivo Experiments). In vivo MRI data were collected using 13 normal rats (Wistar, 210–370 g, Orient Bio, Korea). Animals were initially anesthetized with 3 % isoflurane in a mixture of 30 % O_2 and 70 % N_2O. During MRI acquisition, the isoflurane level was maintained at 1.5–2.0 % to keep the respiratory rate between 50 and 70 breaths/min. A rectal temperature probe and respiration pad (SA Instruments, USA) were used to monitor the temperature and respiration rate, respectively. Body temperature was kept constant within 37 ± 1 °C by circulating warm water through the animal bed.

2.2. Contrast agent

Detailed characteristics of the SPIONs used as the CA in this work are documented in a previous study. (Jung et al., 2014) The core size distribution of the iron oxide was 5–10 nm, and the mean hydrodynamic diameter of the iron oxide nanoparticles was 20 ± 7 nm. The relaxivities r_1 and r_2 of the SPIONs were 2.36 $mM^{-1}s^{-1}$ and 32.94 $mM^{-1}s^{-1}$, respectively, at 7 T. The core and hydrodynamic size distributions of the synthesized SPIONs were determined by transmission electron microscopy (TEM) and the scattering intensity distribution in a dynamic light scattering experiment, respectively. As shown in Supplementary Fig. 1, the concentration of SPIONs in the various brain regions was maintained over at least 100 min post-injection, which is in agreement with a previous work. (Jung et al., 2014)

2.3. In vivo rat brain MRI experiments

All MRI acquisitions were performed with a Bruker Biospec 7 T scanner using a 40 mm transmit/receive volume coil. An animal was placed prone in the animal cradle with the head fixed with a bite bar and nose cone, and the rat brain was positioned as close as possible to the isocenter of the magnet. A catheter (27 G) filled with saline was inserted into the dorsal tail vein of the animal to enable the injection of the CA, comprising SPIONs at 300 μmol Fe/kg. Injections were delivered manually by the same experimenter. All images were acquired in axial orientation, and attempts were made to image the same slice location in each rat. Fat suppression was applied in all MRI sequences.

2.3.1. Experiment 1: resolution dependence of steady-state VSI MRI

In vivo brain imaging was performed on 13 rats ($n = 13$). Experiment 1 consisted of gradient echo (GRE) MRI for ΔR_2^* mapping and spin echo (SE) MRI for ΔR_2 mapping. Both GRE- and SE-MRI were acquired at two in-plane resolutions: 125 × 125 μm^2 and 250 × 250 μm^2.

For the high-resolution (125 × 125 μm^2) scans, the following parameters were used: GRE with a TR of 1.5 s, TE of 9.2 ms, flip angle (FA) of 60°, a receiver bandwidth of 100 kHz, a matrix size of 128 × 128, and 10 averages; SE with a TR of 3 s, TE of 16 ms, a receiver bandwidth of 50 kHz, a matrix size of 128 × 128, and 4 averages.

For the low-resolution (250 × 250 μm^2) scans, GRE was performed with a TR of 1.5 s, TE of 9.2 ms, FA of 60°, a receiver bandwidth of 100 kHz, a matrix size of 64 × 64, and 10 averages; SE was performed with a TR of 3 s, TE of 16 ms, a receiver bandwidth of 50 kHz, a matrix size of 64 × 64, and 4 averages.

Both resolutions used a slice thickness of 1.5 mm, and 8 slices were acquired. The field of view was 16 × 16 mm^2 for both resolutions. The slice coverage extends from +4.76 mm to −7.11 mm relative to the bregma, encompassing key brain regions relevant to VSI study, including major cortical areas, subcortical structures, and the hippocampus. The slice coverage in this study consistent with other rodent VSI MRI studies. (Tropres et al., 2001; Packard et al., 2003; Badruddoja et al., 2003; Troprès et al., 2004; Quarles and Schmainda, 2007) The use of anisotropic voxels (slice thickness > 1000 μm) allows us to achieve high in-plane resolution while maintaining adequate SNR and reasonable scan times. Our approach is consistent with several previous studies in the field. (Tropres et al., 2001; Valable et al., 2008; Packard et al., 2003; Badruddoja et al., 2003; Troprès et al., 2004; Quarles and Schmainda, 2007; Beaumont et al., 2009)

Images were acquired before and after injection of SPIONs (300 μmol Fe/kg), with a 5-minute delay between the injection and subsequent scans. The scan times for GRE MRI were 32 min and 16 min for 125 × 125 μm^2 and 250 × 250 μm^2 resolutions, respectively, while the corresponding scan times for SE MRI were 26 min and 13 min.

Although the low-resolution images have a higher SNR (× 2) from larger voxel volumes with identical bandwidths between resolutions for each sequence type (GRE and SE), they exhibit more pronounced partial volume effects and spatial blurring, particularly at tissue interfaces.

2.3.2. Experiment 2: correction for SPION washout effects

Rats ($n = 5$ for GRE, $n = 4$ for SE) were imaged at least 2 weeks after Experiment 1 to ensure complete clearance of SPIONs from rat plasma. The decrease in ΔR_2^* and ΔR_2 over time after SPION injection was measured by performing high resolution (125×125 μm^2 in-plane resolution) GRE and SE MRI separately over a 2 h period with the same imaging parameters as in Experiment 1, except for scan averaging (specifically, no scan averaging was applied in Experiment 2).

2.4. Data processing

Data were processed in a MATLAB (MathWorks Inc., USA) environment and with Advanced Normalization Tools (ANTs). (Avants et al., 2009)

2.4.1. Anatomical normalization of rat brain MRI

Low resolution (250×250 μm^2 in-plane resolution) MRI images were up-sampled to 125×125 μm^2 by zero-filling the k-space high-frequency region. Image shifts due to head movement during MRI scans were corrected on a slice-by-slice basis using two-dimensional rigid body registration based on high resolution (125×125 μm^2) T_2-weighted (pre-SPION SE) images as stationary images. MRI template images were constructed by selecting the high resolution T_2-weighted image slices from individual scans that best fit the re-sliced Waxholm Space rat brain atlas (Papp et al., 2014) (39×39 μm^2 in-plane resolution with 1500 μm slice thickness). Five continuous slices of MRI data (+1.79 mm to −4.14 mm relative to the bregma, Fig. 1) were included in further analysis to cover the cortex, corpus callosum, striatum, hippocampal formation, and thalamus regions (Supplementary Fig. 2). MRI template images were co-registered to the Waxholm Space atlas of the rat brain based on the antsRegistrationSyN function in ANTs, and then the regions of interest (ROIs) of the cortex, corpus callosum, striatum, hippocampal formation, and thalamus were determined by transforming the pre-defined ROIs of the Waxholm Space rat brain atlas into the MRI template domain. All rat MRI scans were co-registered to the MRI template space using the antsRegistrationSyN function. The linear interpolation option was selected to minimize data contamination during the normalization process. ΔR_2^* and ΔR_2 maps of two different resolutions (125×125 μm^2 and 250×250 μm^2) were first generated (see the following ΔR_2^*, ΔR_2, and VSI calculation section) using motion-corrected MRI images and then transformed into the MRI template space to minimize error propagation due to nonlinear image transformations during the brain normalization. VSI maps were generated by combining ΔR_2^* and ΔR_2 maps in the MRI template space. Average ΔR_2^*, ΔR_2, and VSI maps of 13 rats were generated by spatially averaging the obtained maps in the MRI template domain.

Region-specific analysis of resolution-dependent VSI overestimation was conducted by comparing the percentage differences in ΔR_2^*, ΔR_2, and VSI values between 250 μm^2 and 125 μm^2 resolutions across five brain regions. The differences were plotted against the corresponding VSI values at 125 μm^2 for each voxel. Weighted averages of the percentage differences in VSI values for each brain region were also calculated to illustrate the overall trend of VSI overestimation, with error bars representing the standard error of the mean.

2.4.2. ΔR_2^*, ΔR_2, and VSI calculation

Vessel size index (μm) was estimated as:(Tropres et al., 2001)

$$VSI = 0.425\left(\frac{ADC}{\gamma \Delta\chi B_0}\right)^{\frac{1}{2}}\left(\frac{\Delta R_2^*}{\Delta R_2}\right)^{\frac{3}{2}}, \quad (1)$$

where γ is the ^{1}H gyromagnetic ratio, B_0 is the static magnetic field, ADC is the apparent diffusion coefficient of water in the imaging voxel (here we adopted an ADC of 700 μm^{2}s^{-1} for in vivo VSI calculation), and $\Delta\chi$ is the increase in blood magnetic susceptibility due to the CA. Eq. (1) is valid for the static dephasing regime (SDR). The changes in transverse relaxation rates ΔR_2^* and ΔR_2 due to the injection of SPIONs in blood plasma were derived from measurements made at a single echo time (TE):

$$\Delta R_2^{(*)} = -\frac{1}{TE}\ln\frac{S_{post}}{S_{pre}}, \quad (2)$$

where S_{pre} and S_{post} are the signal intensity before and after administration of the CA, respectively.

2.4.3. $\Delta\chi$ estimation

Magnetic susceptibility values are reported in parts per million (ppm). While these values are derived from measurements in the CGS (centimeter-gram-second) system, the ppm notation is dimensionless and thus independent of the unit system. For reference, to convert between SI and CGS units of volume magnetic susceptibility, the relationship $\chi(SI) = 4\pi \times \chi(CGS)$ can be used. The value of experimental $\Delta\chi$ (0.285 ppm) was evaluated (Yablonskiy and Haacke, 1994) by measuring high resolution steady-state ΔR_2^* values in the cortex region

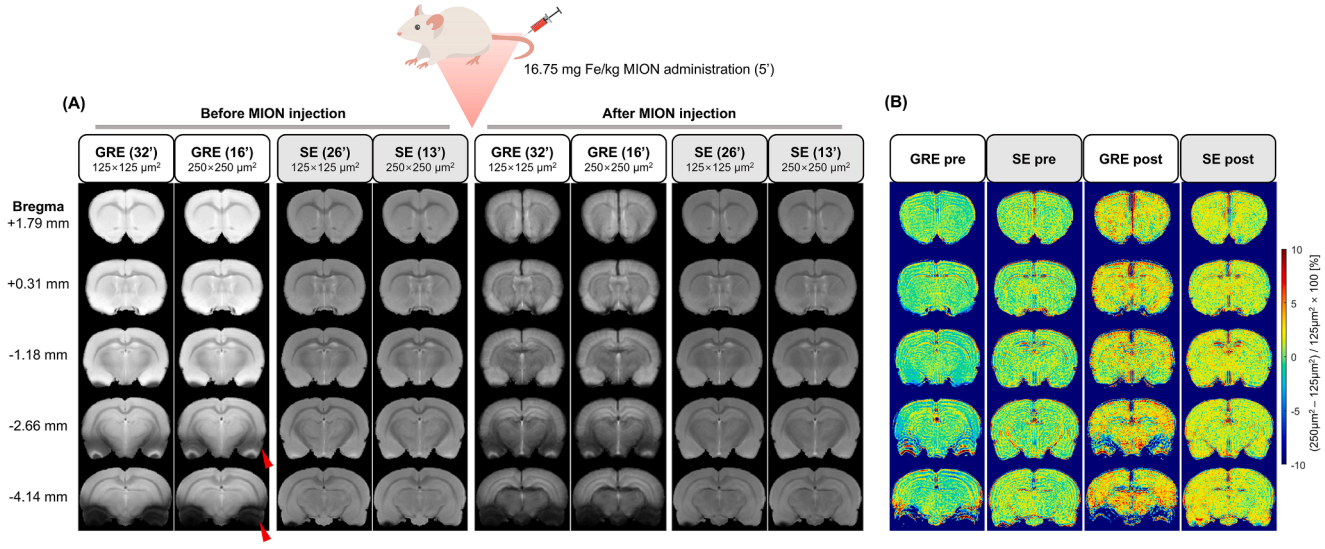

Fig. 1. Dual-resolution gradient echo (GRE) and spin echo (SE) MRI images of in vivo rat brains ($n = 13$ rats) before and after injection of SPIONs. (A) The MRI image of each rat was co-registered and averaged. (B) Percentage difference maps as the spatial resolution decreases ((250 μm^2 − 125 μm^2) / 125 μm^2 × 100 [%]).

(assuming a constant BVf, ξ_{cortex}, of 2.9 %): (Schlageter et al., 1999)

$$\Delta\chi = \frac{3}{4\pi}\frac{\Delta R^{*}_{2,\mathrm{cortex}}}{\xi_{\mathrm{cortex}}\gamma B_0} \quad (3)$$

Considering the injection dose of iron (16.75 mg/kg), a previously suggested estimate of $\Delta\chi$ is 0.4 ppm. (Kim et al., 2013)

2.4.4. SPION washout effect correction

For each time point, mean values of ΔR_2^* ($n = 5$) and ΔR_2 ($n = 4$) were calculated for the ROIs (cortex, corpus callosum, striatum, hippocampal formation, and thalamus). The decline in ΔR_2^* and ΔR_2 due to contrast washout was assessed by fitting the best linear lines to $\Delta R_2^{(*)}$–time data points for each ROI (see Supplementary Fig. 1). The correction factor (− slopes of the fitted lines × time duration after SPION injection) was added to the mean $\Delta R_2^{(*)}$ values for each ROI.

2.5. Numerical simulations

Monte Carlo proton diffusion simulations were conducted to investigate the resolution dependence of VSI MRI. Changes in the magnetic resonance transverse relaxation rates (ΔR_2^* and ΔR_2) resulting from the intravascular CA were computed using established procedures at a B_0 of 7 T. (Lee et al., 2020) To model susceptibility-based contrast mechanisms, the finite perturber method was utilized. (Pathak et al., 2008) This approach calculated the B_0 shift for randomly distributed cylindrical models (refer to Fig. 2A) with various radii (each random cylinder model consisted of a single vessel radius of 1, 2, 3, 5, 10, 14, or 20 μm) at BVfs of 3 % and a $\Delta\chi$ of 0.3 ppm. For each combination of radius and BVf, a total of 50 simulation volumes were created, corresponding to 50 simulations each ($n = 50$). Each simulation featured a unique random distribution and orientation of vessels within the simulation volume. The initial placement of spins was uniform, with one spin placed in each grid voxel of the simulation, except for voxels inside the vessel area. The simulation volume was 500 × 500 × 500 μm^3 with a unit voxel size of 1 × 1 × 1 μm^3, and the simulation unit time was 1 ms. The diffusion coefficient used in the simulation was 1000 μm^{2}s^{-1}. TE values for GRE and SE acquisitions were 10 ms and 16 ms, respectively. The GRE echo time in simulations (10 ms) differs slightly from the experimental value (9.2 ms) due to the discrete time steps used in our Monte Carlo simulations. Three independent simulation volumes, each measuring 500 × 500 × 500 μm^3, were randomly selected and stacked to form a single simulation volume of 500 × 500 × 1500 μm^3, representing the 1500 μm slice thickness used in the experiments.

For multi-resolution comparisons, the simulation volume was divided into the following subvolumes: 125 × 125 × 1500 μm^3, 250 × 250 × 1500 μm^3, and 500 × 500 × 1500 μm^3. The phase accumulation of each proton during TE was calculated, and S_{post} was determined by averaging the accumulated phase factor across the entire ensemble of diffusing protons in the simulation volume. ΔR_2^*, ΔR_2, and VSI for each volume size were calculated using Eq. (1) and (2), with S_{pre} set to 1.

An additional simulation was carried out using a unidirectional and

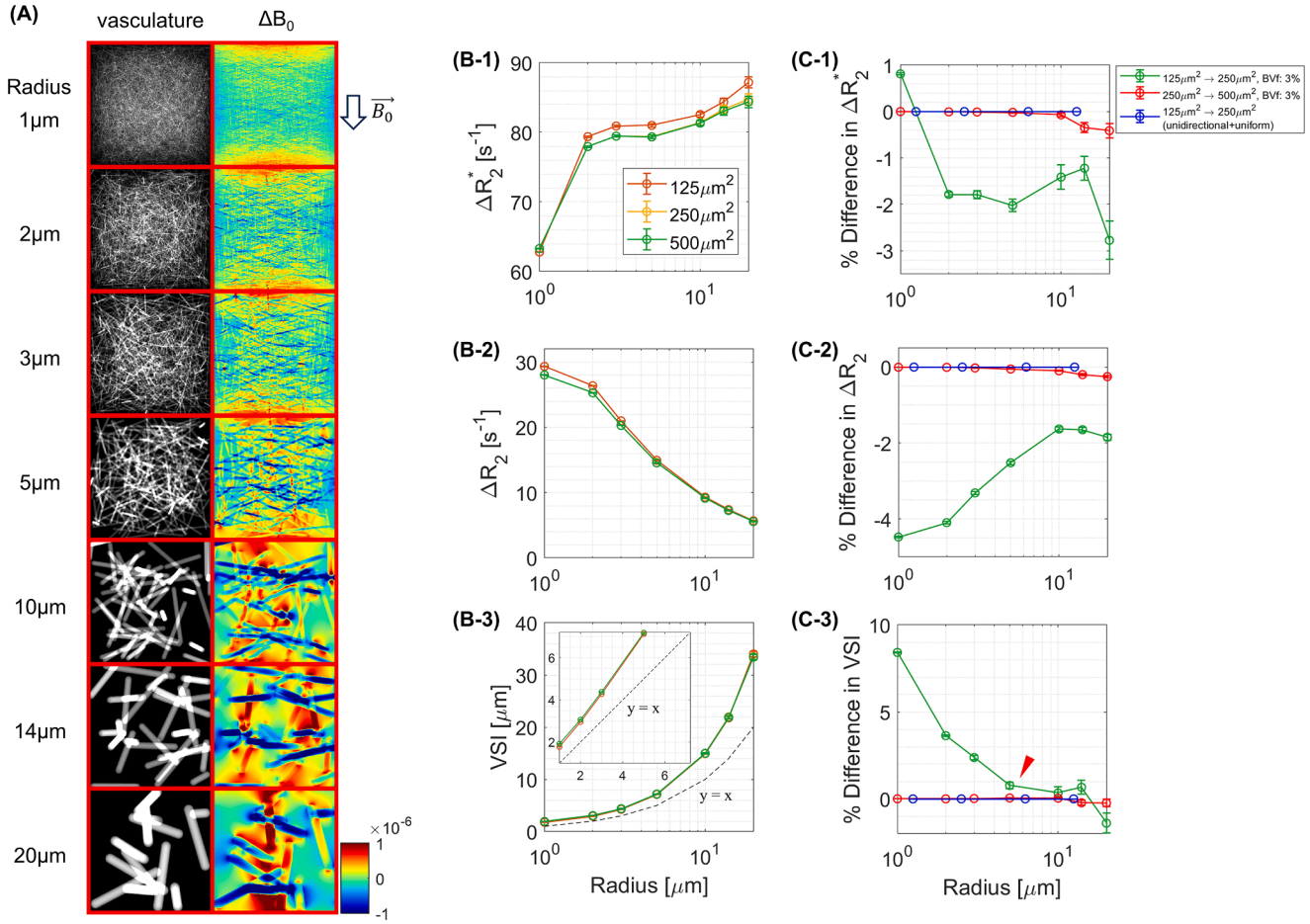

Fig. 2. Simulation results for randomly distributed and unidirectional+uniform cylindrical models. (A) Representative randomly distributed cylindrical models with various radii and calculated ΔB_0 for Monte Carlo proton diffusion simulation. (B) ΔR_2^*, ΔR_2, and VSI values at BVf of 3 %. (C) Percentage differences in ΔR_2^*, ΔR_2, and VSI between different spatial resolutions for randomly distributed (red and green) and unidirectional+uniform (blue) models. The red arrow highlights the condition comparable to those used in VSI experiments. The lack of resolution dependence in the unidirectional+uniform model highlights the role of vessel distribution in VSI resolution sensitivity.

uniformly distributed cylinder model to investigate the resolution dependence of VSI MRI in a negative-control scenario, as shown in Supplementary Fig. 3. The cylinder model had radii of 1.25, 2.5, 6.25, and 12.5 μm with a BVf of 3.14 %. The simulation volume size was 250 × 250 × 250 μm^3, and the unit voxel size was 0.25 × 0.25 × 0.25 μm^3. The resolution dependence of ΔR_2*, ΔR_2, and VSI was evaluated for sub-volumes of 125 × 125 × 250 μm^3 and 250 × 250 × 250 μm^3.

3. Results

3.1. Anatomical normalization of rat brain MRI

Fig. 1A displays averaged MRI images of rat brains (n = 13, +1.79 mm to −4.14 mm relative to the bregma) after registration with the rat brain atlas maintaining the detailed anatomy of the brain. The low-resolution images, while having higher SNR, show more noticeable partial volume effects and spatial blurring, especially at tissue interfaces. Regions outside the brain were manually removed to focus on the brain ROIs. Because of the GRE image signal voids near the bone–tissue interface in later slices, as indicated with red arrows in the figure, these regions were excluded from the ROI-based analysis.

Fig. 1B shows percentage difference maps from reduced spatial resolution ((250 μm^2 – 125 μm^2) / 125 μm^2 × 100 [%]) for GRE and SE images before and after injection of the CA. Overall, the percentage difference maps of GRE and SE images appear more pronounced after CA injection compared to those before injection, indicating that the resolution dependence stems mainly from the effect of inhomogeneous field variations due to the intravascular CA.

3.2. MC simulation

Susceptibility difference-induced B_0 shift maps from MC simulations with randomly distributed cylindrical models are shown in Fig. 2A. For cylinder radii of 1, 2, 3, 5, 10, 14, and 20 μm filled with a BVf of 3 %, the ΔR_2*, ΔR_2, and VSI values were computed and plotted for in-plane resolutions of 125 × 125 μm^2 , 250 × 250 μm^2 , and 500 × 500 μm^2 (Fig. 2B). ΔR_2* shows an increase with the cylinder radius, reaching a plateau at a radius of 2 μm as shown in Fig. 2B-1, while ΔR_2 is observed to gradually reduce in value as the radius increases, as shown in Fig. 2B-2. In Fig. 2B-3, VSI tends to increase as a function of cylinder radii and be overestimated compared to the true vessel radius (inset of Fig. 2B-3). These trends of ΔR_2*, ΔR_2, and VSI are consistent with previous findings. (Troprès et al., 2015) Overall, both ΔR_2* and ΔR_2 for a spatial resolution of 125 × 125 μm^2 were higher than those at other spatial resolutions. To further investigate this spatial resolution dependence, the percentage differences of ΔR_2*, ΔR_2, and VSI were calculated by the following equation and plotted in Fig. 2C: % (percentage) difference = (values at low resolution − values at high resolution) / (values at high resolution) × 100.

As the spatial resolution decreased from 125 × 125 μm^2 to 250 × 250 μm^2 , the percentage difference in ΔR_2* values increased in negative value for radii between 2 and 10 μm, as shown in Fig. 2C-1. Whereas, the percentage difference in ΔR_2 values reached the largest negative value at the 1 μm radius, gradually decreased up to 10 μm, and again increased at the 20 μm radius, as shown in Fig. 2C-2. The percentage difference of VSI showed a positive increase because that of ΔR_2 was larger than for ΔR_2*, where the estimation of VSI is derived using both ΔR_2 and ΔR_2* values. Specifically, the percentage difference of VSI exhibited a half U-shaped pattern, with peaks at small (1 μm) and large radii (20 μm) and a minimum between 4 and 10 μm, as shown in Fig. 2C-3.

For comparison, we also simulated a unidirectional and uniformly distributed vessel model (Supplementary Fig. 3), shown as blue lines in Fig. 2C. In contrast, in the case of the unidirectional and uniformly distributed cylindrical model, reducing the resolution from 125 × 125 μm^2 to 250 × 250 μm^2 did not alter ΔR_2*, ΔR_2, and VSI for the various vessel radii, as shown in Fig. 2C-3 with blue lines and open circles. As the spatial resolution further decreased from 250 × 250 μm^2 to 500 × 500 μm^2, there were no significant percentage differences between ΔR_2 and ΔR_2* for all radii, resulting in no observable alterations in VSI values. This difference underscores the importance of vessel distribution in determining resolution-dependent effects on VSI measurements.

3.3. In vivo rat brain ΔR_2*, ΔR_2, and VSI maps

Fig. 3 presents voxel-wise maps of ΔR_2*, ΔR_2, and VSI along with corresponding percentage difference maps between 125 μm^2 and 250 μm^2 spatial resolutions (n = 13). ROI templates for the cortex, corpus callosum, striatum, hippocampal formation, and thalamus are superimposed in Fig. 3A excluding the areas with severe field inhomogeneity near the bone–tissue interface. In Fig. 3B,C, the percentage difference of ΔR_2* is smaller than that of ΔR_2 for all brain regions. In Fig. 3C,D with red arrows, the percentage difference map of ΔR_2 revealed negative increases in the corpus callosum area and in some portion of the hippocampal formation region, resulting in a positive increase in VSI.

To specify distinct regional differences in ΔR_2, ΔR_2*, and VSI values with varying spatial resolutions, Fig. 4 zooms in ΔR_2, ΔR_2*, and VSI maps for close examination. For the ventricle and sinus regions shown in Fig. 4A and 4 B, the percentage difference maps of ΔR_2 and ΔR_2* exhibit spill-in (ventricle) and spill-out (sinus) phenomena, respectively, due to well-known partial volume effects as indicated by black arrows. These partial volume effects were observed to be mitigated in the corresponding percentage difference map of VSI.

In the case of the area near the corpus callosum and hippocampal formation regions as shown in Fig. 4C, the percentage difference map of ΔR_2 exhibited more significant reductions for small (white dotted lines) and slightly larger (blue dotted lines) vessels, and consequently the percentage differences in VSI values were significantly increased. On the other hand, macrovessels (black arrow with yellow enclosures) showed smaller VSI changes compared to those from smaller vessels.

To further understand the causes of the resolution dependence of VSI, Fig. 5 presents a scatter plot of the percentage difference values of a representative slice containing the corpus callosum, hippocampal formation, and cortex regions against the corresponding experimentally measured VSI values at 125 μm^2 . As shown in Fig. 5A, significant positive percentage differences in VSI values (indicating larger VSI values at 250 μm^2 compared to those at 125 μm^2) were observed in small vessel regions (VSI < 5 μm), along with corresponding negative percentage differences in ΔR_2 values. Decreasing percentage differences in VSI values were noted as VSI values increased up to approximately 10 μm. However, when VSI values exceeded 10 μm, an increase in the percentage differences in VSI was again observed.

In Fig. 5B, the simulated percentage differences in ΔR_2*, ΔR_2, and VSI are superimposed on the corresponding experimental measurements, showing a generally similar trend. The overestimation ratio obtained from the simulation results (shown in the inset of Fig. 2B-3) was used to adjust the experimental VSI values for comparison with the simulation results. The need for this correction arises from the known tendency of VSI measurements to overestimate actual vessel sizes, as demonstrated in previous studies. (Tropres et al., 2001; Kiselev et al., 2005) To align the experimental VSI values with the simulation input radii, a correction factor (Fig. 5D) was applied. This correction factor was calculated as the ratio between the mean simulated VSI value and the mean simulation input radius across all vessel sizes. This adjustment accounts for the systematic overestimation of VSI in our measurements compared to the actual vessel sizes (Fig. 5C,D). The ΔR_2, ΔR_2*, and VSI values between spatial resolutions of 125 μm^2 and 250 μm^2 (n = 13) were then compared for the brain ROIs, as shown in Fig. 6. A minimal decrease in mean ΔR_2* (< 3 %) was observed for all ROIs without significant changes in the shape of the distributions as the resolution decreased (Fig. 6A,D). However, there was an apparent decrease in the mean ΔR_2 of the corpus callosum (−9.8 %) and hippocampal formation (−8.1 %) regions. These regions were observed to have small VSI value

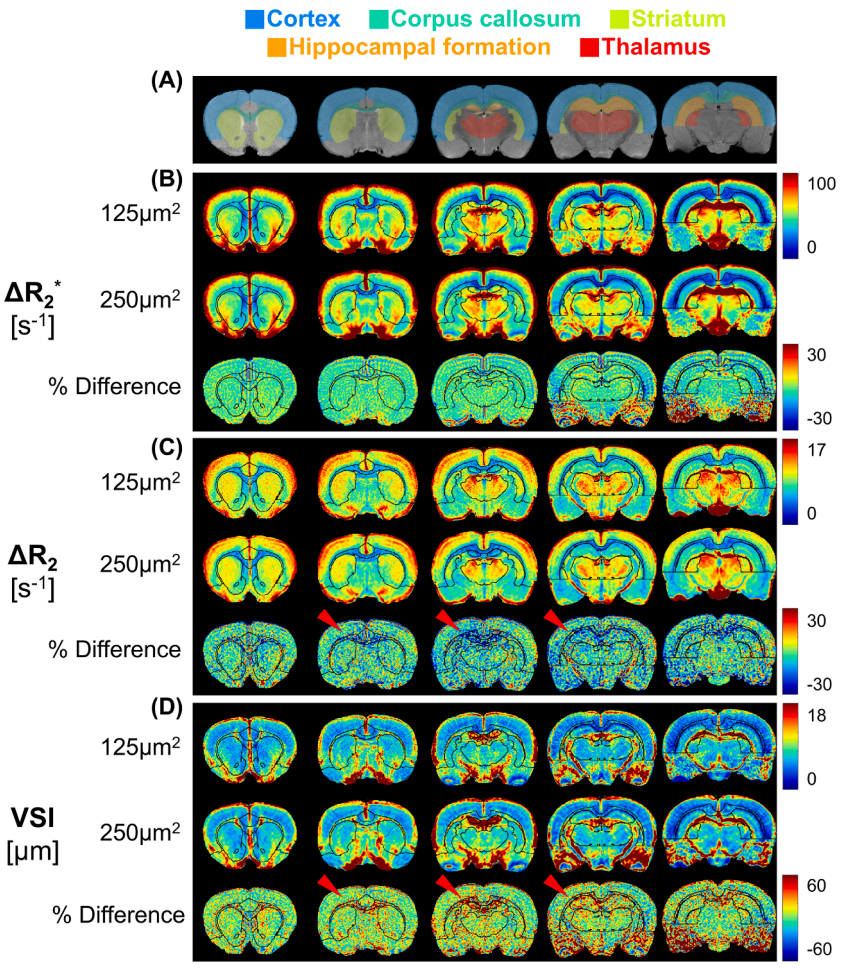

Fig. 3. Comparison of averaged ΔR_2^*, ΔR_2, and VSI maps of 13 rats at in-plane resolutions of 125 μm² and 250 μm². (A) Colored brain ROIs overlaid on T_2-weighted SE images. Five selected slices of (B) ΔR_2^*, (C) ΔR_2, and (D) VSI maps and their percentage difference as the in-plane resolution decreased from 125 μm² to 250 μm².

populations (< 5 μm) compared to other brain regions, as indicated by the red circles in the figure. As a result, increased mean VSI values were observed for the corpus callosum (12.2 %) and hippocampal formation (12.0 %) regions compared to other brain regions.

To further investigate the effect of vessel size on the overestimation of regional VSI values, Fig. 7 displays a scatter plot of the percentage differences in ΔR_2^*, ΔR_2, and VSI values for five different brain regions against the corresponding experimental VSI values at 125 μm². Analysis revealed positive percentage differences in VSI values across all regions when VSI was smaller than approximately 10 μm. This provides evidence for the overestimation of VSI values at lower resolutions for smaller vessels.

The hippocampal formation and corpus callosum regions exhibited larger weighted averages of percentage differences in VSI values compared to other regions, albeit for different reasons. In the hippocampus, this can be attributed to the higher populations of small vessels. (Kolinko et al., 2021; Cavaglia et al., 2001; Grivas et al., 2003) For the corpus callosum, despite its lower vascular density (Cavaglia et al., 2001), the large percentage differences in VSI values are likely due to two factors: (1) the heightened sensitivity of VSI measurements to smaller vessels, which predominate in this region, and (2) the high diffusion coefficient characteristic of white matter structures. Our simulation results indicate that percentage differences in VSI are more pronounced for smaller vessels and in regions with high diffusion coefficients (Supplementary Fig. 6). In the hippocampal formation region, such resolution-dependent overestimations were also apparent for larger (> 10 μm) vessels as well, showing a half U-shaped trend consistent with the simulation results. Fig. 7B highlights these trends, illustrating the regional variability in the extent of VSI overestimation and emphasizing the significant impact of vessel size on the accuracy of VSI measurements.

To investigate the impact of diffusion coefficient on VSI measurements, we performed additional simulations using diffusion coefficients of 700 μm²/s, 1000 μm²/s, and 1300 μm²/s (Supplementary Fig. 6). This range encompasses the in vivo ADC value used for VSI calculations (700 μm²/s) and extends to higher values to explore the full spectrum of potential diffusion effects. As ADC values increases, it is observed that the "% difference in VSI" exhibits a slight upward trend while maintaining a consistent overall pattern.

As shown in Supplementary Fig. 7, at very fine resolutions (<50 μm²), no significant variations are observed with changes in resolution. However, when the resolution exceeds ~50 μm², apparent percentage differences in VSI emerge. A notable decrease in ΔR_2 is observed when the resolution exceeds ~125 μm², attributed to significant changes in the averaged phase distribution between 125 μm² and 250 μm², as shown in Supplementary Fig. 4. Resultingly, the percentage difference in VSI becomes more weighted towards small vessel radii. Beyond ~500 μm², no further significant variations are observed.

4. Discussions and conclusions

4.1. Insights from MC simulations and correspondence with experiments

This study utilized Monte Carlo simulations to analyze susceptibility

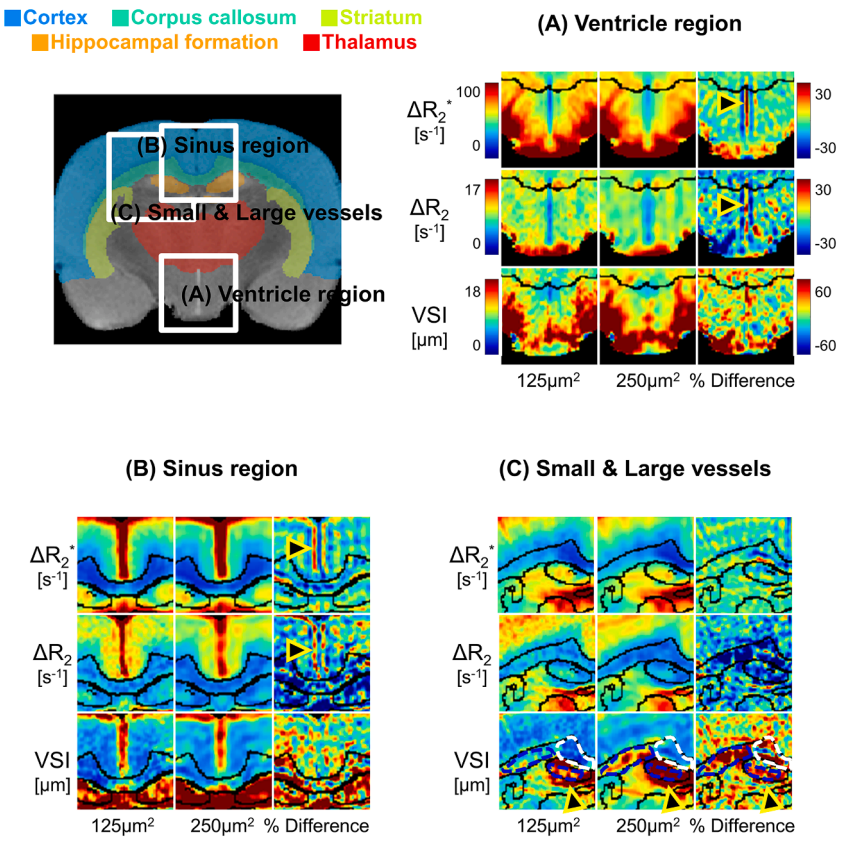

Fig. 4. Representative rat brain regions showing (A) spill-in partial volume effects of ventricles, (B) spill-out partial volume effects of large vessels, and (C) small and large VSI regions.

difference-induced B_0 shift maps with randomly distributed cylindrical models, examining how vessel radius and spatial resolution impact ΔR_2*, ΔR_2, and VSI. The results for cylinder radii from 1 to 20 μm and spatial resolutions of 125 × 125 μm^2, 250 × 250 μm^2, and 500 × 500 μm^2 indicated that ΔR_2* increased with vessel radius up to 2 μm, then plateaued. Conversely, ΔR_2 decreased as vessel radius increased. VSI was consistently overestimated relative to true vessel size. Percentage difference analysis revealed that reducing the resolution from 125 × 125 μm^2 to 250 × 250 μm^2 led to larger negative differences in ΔR_2* and ΔR_2, particularly for intermediate vessel sizes (2–10 μm). VSI differences showed a half U-shaped pattern, peaking at the smallest and larger vessel sizes (> 10 μm).

In vivo rat brain analyses mirrored these findings. Specifically, in vivo rat brain VSI MRI revealed brain regional differences in the changes in ΔR_2*, ΔR_2, and VSI as the spatial resolution decreased from 125 μm^2 to 250 μm^2. Spill-in and spill-out partial volume effects were observed for ΔR_2* and ΔR_2 in the ventricles and sinus, respectively; however, these effects were mitigated in VSI. It is noted that decreases in ΔR_2 were pronounced in small vessels while minimal changes were observed for ΔR_2*, leading to increased VSI in the corpus callosum and hippocampal formation regions. Although the p-values from the Wilcoxon rank-sum test indicate statistical significance for the VSI distribution differences at different resolutions across all ROIs of interest (Fig. 6), this result is likely influenced by the large sample size. However, the small mean VSI differences (<10 %) in certain areas may have limited practical significance in experimental applications. This trend was linked to higher populations of small vessels, which contributed to the VSI overestimation in these regions. The experimental observations were consistent with the MC simulations using various cylinder radii, which showed that significant differences existed between spatial resolutions of 125 μm^2 and 250 μm^2 but not between 250 μm^2 and 500 μm^2 , which are commonly used resolutions for preclinical rat brain MRI studies.

In contrast, in the case of a unidirectional and uniformly distributed cylindrical model (Supplementary Fig. 3), reducing the resolution from 125 × 125 μm^2 to 250 × 250 μm^2 did not alter ΔR_2*, ΔR_2, and VSI for various vessel radii, as shown in Fig. 2C with the blue lines and open circles. Such results suggest that the origin of the VSI changes between spatial resolutions of 125 μm^2 and 250 μm^2 is likely from the inhomogeneous field distribution from randomly oriented in vivo capillary vessels.

The simulation also showed minimal changes in the VSI values between 250 μm^2 and 500 μm^2. This indicates that the difference in ΔR_2 may be the primary factor influencing VSI differences, and it also suggests that the averaged phase distribution varies between the resolutions (125 μm^2 and 250 μm^2). Specifically, as the spatial resolution changes, there was a significant change in the distribution of the averaged phase between 125 μm^2 and 250 μm^2, as shown in Supplementary Fig. 4. However, at larger resolutions, the distribution of the averaged phase tended to normalize. This normalization means that the differences in VSI values become less substantial beyond 250 μm^2, which minimizes further changes in VSI values even when the resolution decreases to 500 μm^2. This stabilization indicates that decreasing the resolution beyond a certain point does not significantly affect VSI measurements, likely because the underlying distribution of the measured parameter reaches a stable state. It is noted that the shift in VSI behavior observed between 20 and 125 μm^2 resolution also underscores a critical range where VSI measurements are highly sensitive to resolution changes as well. However, direct experimental validation at these high resolutions is limited and these simulation findings as shown in Supplementary Fig. 7 can inform future research on optimizing resolution selection for targeting specific vessel size ranges.

Scatter plots comparing the percentage differences in VSI values against vessel size for different brain regions consistently demonstrated a pronounced overestimation for small vessels (< 5 μm) and a half U-

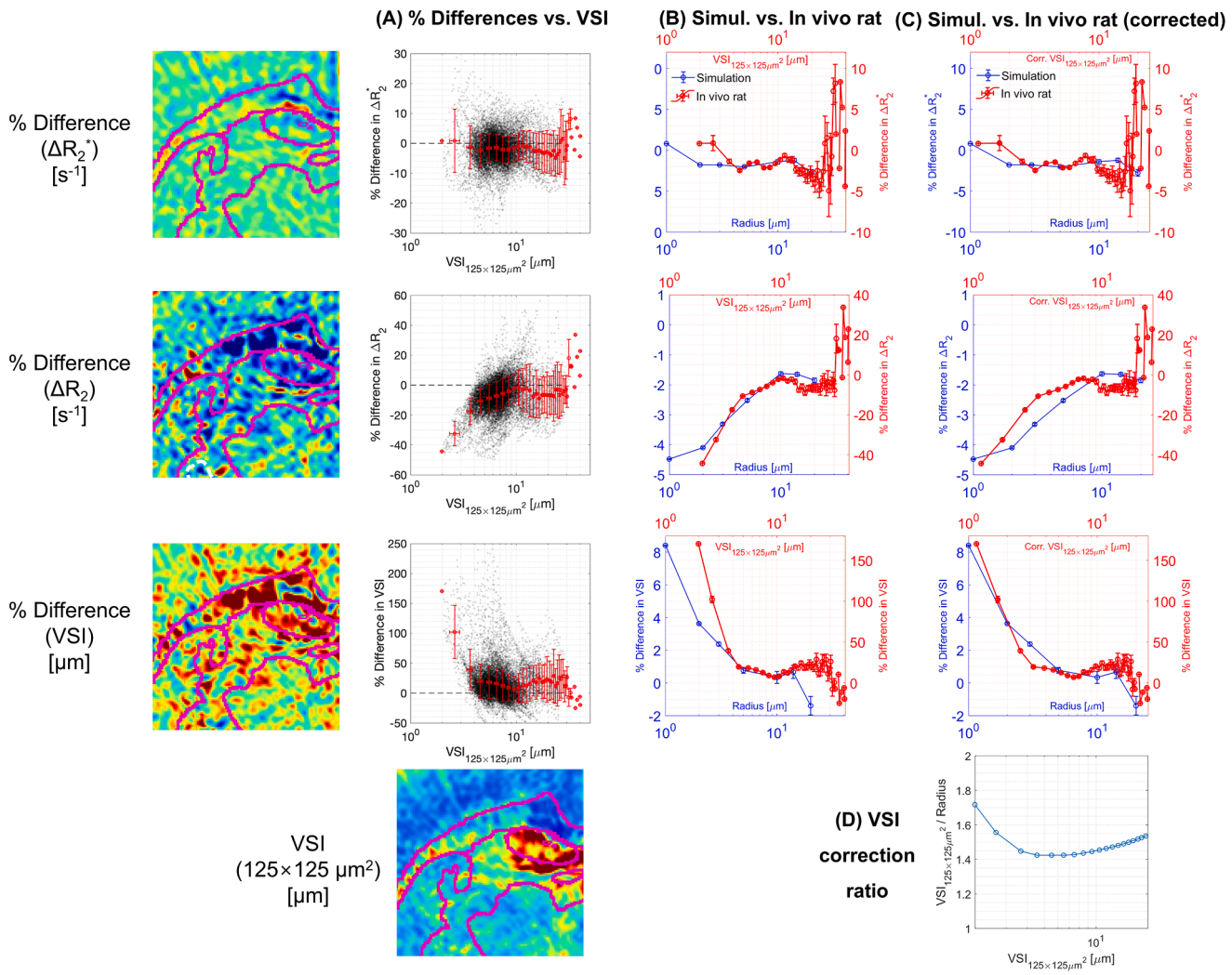

Fig. 5. Comparison between the in vivo percentage difference of VSI and Monte Carlo simulation. Since the simulation did not account for partial volume effects, a representative slice containing the corpus callosum, hippocampal formation, and cortex regions was compared without the influence of partial volume effects from large vessels and ventricles. (A) Percentage differences in ΔR_2*, ΔR_2, and VSI scatter-plotted against the corresponding experimentally measured VSI values at 125 μm^2 . (B) Comparison of percentage difference scatter plots between experiment and simulation. (C) Comparison of percentage difference scatter plots between experiment and simulation with the experimental VSI corrected by (D) the VSI correction ratio.

shaped trend for regions including larger vessels (especially for the hippocampal formation region). These patterns were consistent across different brain regions, emphasizing the impact of spatial resolution and vessel size on the accuracy of VSI quantification. This study highlights the need to consider these factors when interpreting VSI data, particularly in regions with a high density of small vessels.

The correction applied to align experimental VSI values with simulation input radii (Fig. 5C,D) provides valuable insights into the relationship between measured VSI and actual vessel sizes. This adjustment accounts for the systematic overestimation of VSI in our measurements compared to the actual vessel sizes, a phenomenon consistently observed in previous studies. (Tropres et al., 2001; Kiselev et al., 2005) It's important to note that the correction does not change the relative differences observed between different vessel sizes or spatial resolutions. The trends and patterns in our data remain consistent, with or without this correction.

4.2. Origins of resolution dependence in vsi measurements

The resolution dependence observed in VSI measurements likely stems from a complex interplay of factors that challenge some of the underlying assumptions of the technique. One key consideration is the potential violation of the static dephasing regime, particularly for smaller vessels where diffusion effects become more pronounced. This violation may occur to varying degrees at different spatial resolutions, contributing to the observed resolution-dependent effects.

Another critical factor is the heterogeneity of vessel sizes within a given voxel. As spatial resolution changes, the ability to capture this heterogeneity also varies, potentially leading to differential effects on VSI estimates. Higher resolutions may better represent the true distribution of vessel sizes, while lower resolutions could result in averaging effects that bias VSI calculations.

While a comprehensive analytical derivation of these effects remains challenging at present, Monte Carlo simulations have provided valuable insights into these resolution-dependent phenomena. These simulations corroborate the experimental findings, demonstrating a clear dependency of VSI estimates on in-plane resolution. Notably, this study systematically investigates resolution effects across a range typically used in preclinical experiments (120–500 μm^2 in-plane, with slice thicknesses exceeding 1000 μm), an aspect that has been largely overlooked in previous VSI studies.

Future work combining advanced analytical models may further elucidate the precise mechanisms underlying resolution dependence in VSI estimates. Such investigations could potentially lead to improved

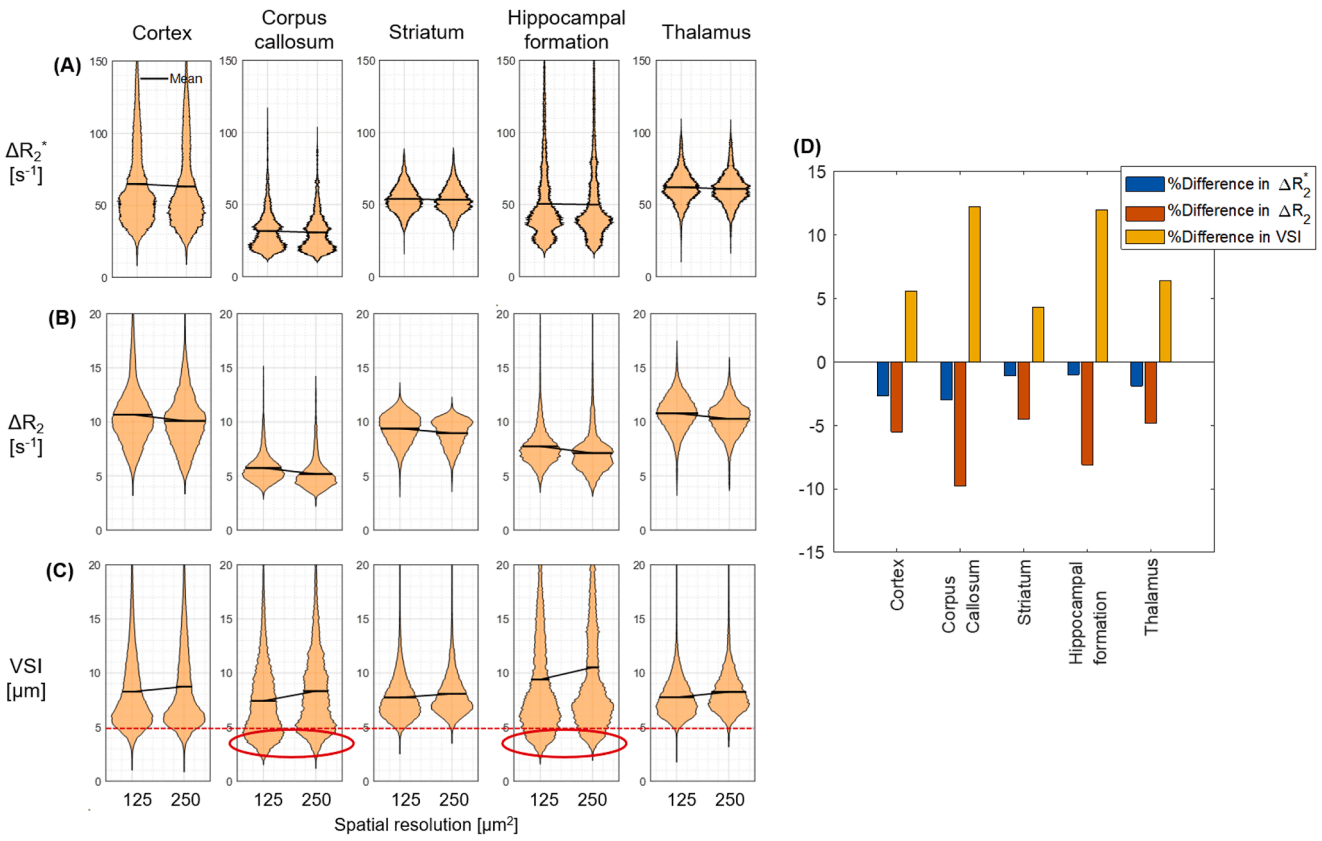

Fig. 6. Comparison of brain regional (A) ΔR_2^*, (B) ΔR_2, and (C) VSI distributions of in vivo rat brains ($n = 13$) at 125 μm² and 250 μm² in-plane resolutions. Statistical analysis using the Wilcoxon rank-sum test indicates that all distributions are significantly different ($p < 0.05$). (D) Percentage difference in mean ΔR_2^*, ΔR_2, and VSI values as the in-plane resolution decreases from 125 μm² to 250 μm². Although the p-values from the Wilcoxon rank-sum test indicate statistical significance for the VSI distribution differences at different resolutions across all ROIs of interest, this result is likely influenced by the large sample size. However, the small mean VSI differences (<10 %) in certain areas may have limited practical significance in experimental applications.

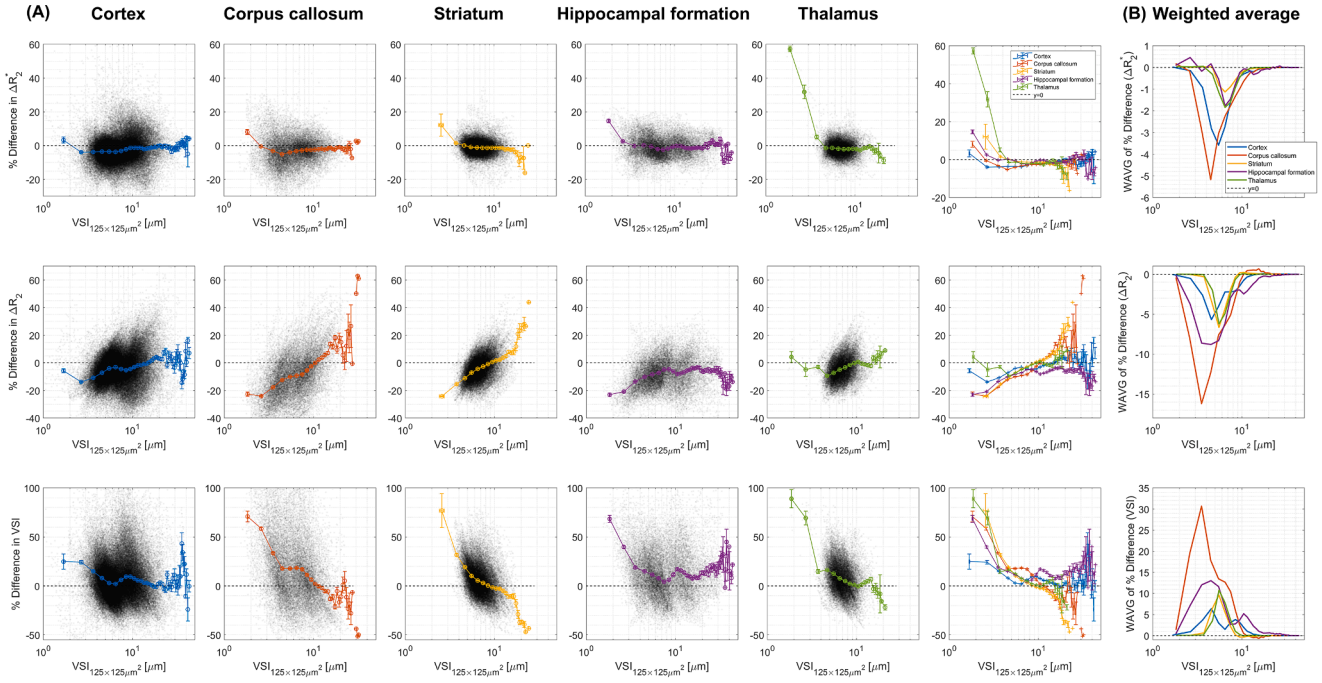

Fig. 7. Region-specific analysis of resolution-dependent VSI overestimation. (A) Scatter plots showing the percentage differences in ΔR_2^*, ΔR_2, and VSI values between 250 μm² and 125 μm² resolutions, plotted against the corresponding VSI values at 125 μm² for five brain regions. Each point represents an individual voxel. (B) Weighted averages of percentage differences in VSI values for each brain region, illustrating the overall trend of VSI overestimation. Error bars represent standard error of the mean.

VSI methodologies that account for these resolution-dependent effects, enhancing the accuracy and reliability of microvascular measurements across different spatial scales.

4.3. Limitations and future work

Since the VSI value is nonlinear with respect to CA concentration, (Tropres et al., 2004) it may not be perfectly corrected even after applying CA washout correction. Although CA washout correction was likely effective here because the ΔR_2^* and ΔR_2 values were experimentally corrected, the nonlinearity remains a challenge. In the MC simulations, VSI was defined as the radius, but the calculated VSI values tended to be larger than the input cylinder radii. This discrepancy highlights the complexity of accurately determining VSI from experimental measurements.

Moreover, it is not clear whether the observed VSI differences due to resolution changes are specific to the steady-state approach or if they also apply to the dynamic approach. The steady-state approach involves conventional GRE- and SE-based readout, while the dynamic approach typically uses spin- and gradient-echo (SAGE) echo planar imaging (EPI). (Bandettini et al., 1994; Pannetier et al., 2012) Further investigation is needed to determine if the resolution dependence of VSI measurements is consistent across both methodologies. This uncertainty underscores the need for a deeper understanding of how different imaging techniques and resolutions impact VSI calculations.

VSI values, particularly ΔR_2, are also influenced by underlying tissue diffusion. (Tropres et al., 2001) Variations in diffusion, including non-Gaussian diffusion that occurs in complex cellular environments, and diffusion anisotropy, which refers to direction-dependent variation in diffusion, can significantly impact VSI measurements as well. (Xia, 1998; Gil et al., 2016) These diffusion characteristics may vary across different brain regions, contributing to regional differences in VSI values at different resolutions. (Oouchi et al., 2007) Accordingly, it is essential to consider the impact of these diffusion variations to fully understand the origin of resolution dependence in VSI quantification, as ignoring these factors could result in an incomplete or inaccurate interpretation of resolution-dependent VSI measurements.

The acquisition strategy employed in this study represents a deliberate trade-off between whole-brain coverage and other critical factors such as slice thickness and SNR. The protocol prioritizes high-quality data acquisition in key brain regions over complete brain coverage. This approach was deemed optimal for addressing the specific research questions, which focus on comparing VSI measurements at different resolutions rather than performing whole-brain analysis.

The use of anisotropic voxels, while consistent with common practices in the field, may introduce some biases in our VSI measurements. The comparison between simulation results at two different slice thickness (500 and 1500 μm) was shown in Supplementary Fig. 5. The results showed similar behavior in small vessels (<10 μm) but revealed some deviations in larger vessels. This deviation likely reflects the increased homogenization of field variations in larger vessels due to greater slice thickness, which makes changes in-plane resolution (from 125 μm^2 to 250 μm^2) less influential on VSI changes in these larger vessels. Future experimental studies could investigate the impact of voxel anisotropy on VSI measurements by comparing results from isotropic and anisotropic acquisitions, potentially using advanced acquisition techniques that allow for high-resolution isotropic imaging within reasonable scan times in rodent models.

5. Conclusion

In summary, we conducted a comprehensive comparison of the spatial resolution–dependent VSI across various brain regions including the cortex, corpus callosum, striatum, hippocampal formation, thalamus, macrovessel area, and ventricles. Our investigation demonstrated that the effect of spatial resolution on VSI varies by region. This variability is primarily due to the differing tendencies of ΔR_2 values with respect to vessel radii. Additionally, our experimental findings showed a clear agreement with simulation results. By aligning the experimental data with simulations, we could better understand the mechanisms driving the resolution dependence of VSI and validate our methodology. Overall, this study underscores the importance of considering spatial resolution when measuring VSI, as different brain regions exhibit unique responses due to their vascular structures. This insight is crucial for accurately interpreting VSI measurements and improving the precision of neuro-microvascular imaging techniques.

CRediT authorship contribution statement

DongKyu Lee: Writing – review & editing, Writing – original draft, Visualization, Validation, Software, Project administration, Methodology, Investigation, Formal analysis, Data curation, Conceptualization. **Yelim Gong:** Writing – original draft, Validation, Methodology, Formal analysis, Data curation, Conceptualization. **Abel Worku Tessema:** Data curation. **SoHyun Han:** Writing – review & editing, Writing – original draft, Visualization, Validation, Supervision, Funding acquisition. **Hyung Joon Cho:** Writing – review & editing, Writing – original draft, Validation, Supervision, Resources, Project administration, Investigation, Funding acquisition, Conceptualization.

Declaration of competing interest

The authors declare that they have no competing financial interests or personal relationships that could have influenced the research in this study.

Acknowledgments

This work was partially supported by grants from the National Research Foundation of the Korean government (RS-2024-00342982 and RS-2024-00508681). This research was also supported by a grant of the Korea Dementia Research Project through the Korea Dementia Research Center (KDRC), funded by the Ministry of Health & Welfare and Ministry of Science and ICT, Republic of Korea (grant number: RS-2024-00334574). This research was also supported by KBRI basic research program through Korea Brain Research Institute funded by Ministry of Science and ICT (24-BR-05-02).

Supplementary materials

Supplementary material associated with this article can be found, in the online version, at doi:10.1016/j.neuroimage.2024.120979.

Data availability

Data will be made available on request.

References

Avants, B.B., Tustison, N., Song, G., 2009. Advanced normalization tools (ANTS). Insight. J. 2 (365), 1–35.

Badruddoja, M.A., Krouwer, H.G., Rand, S.D., Rebro, K.J., Pathak, A.P., Schmainda, K. M., 2003. Antiangiogenic effects of dexamethasone in 9L gliosarcoma assessed by MRI cerebral blood volume maps. Neuro Oncol. 5 (4), 235–243.

Bandettini, P.A., Wong, E.C., Jesmanowicz, A., Hinks, R.S., Hyde, J.S., 1994. Spin-echo and gradient-echo EPI of human brain activation using BOLD contrast: a comparative study at 1.5 T. NMR Biomed. 7 (1-2), 12–20.

Beaumont, M., Lemasson, B., Farion, R., Segebarth, C., Rémy, C., Barbier, E.L., 2009. Characterization of tumor angiogenesis in rat brain using iron-based vessel size index MRI in combination with gadolinium-based dynamic contrast-enhanced MRI. J. Cerebral Blood Flow Metabol. 29 (10), 1714–1726, 35.

Boehm-Sturm, P., Farr, T.D., Adamczak, J., et al., 2013. Vascular changes after stroke in the rat: a longitudinal study using optimized magnetic resonance imaging. Contrastmed. Mol. Imag. 8 (5), 383–392.

Bosomtwi, A., Jiang, Q., Ding, G.L., et al., 2008. Quantitative evaluation of microvascular density after stroke in rats using MRI. J. Cerebral Blood Flow Metabol. 28 (12), 1978–1987.
Bouchet, A., Lemasson, B., Le Duc, G., et al., 2010. Preferential effect of synchrotron microbeam radiation therapy on intracerebral 9L gliosarcoma vascular networks. Int. J. Radiat. Oncol.* Biol.* Phys. 78 (5), 1503–1512.
Boxerman, J.L., Hamberg, L.M., Rosen, B.R., Weisskoff, R.M., 1995. MR contrast due to intravascular magnetic susceptibility perturbations. Magnet. Resonance Med. 34 (4), 555–566.
Cavaglia, M., Dombrowski, S.M., Drazba, J., Vasanji, A., Bokesch, P.M., Janigro, D., 2001. Regional variation in brain capillary density and vascular response to ischemia. Brainresearch 910 (1-2), 81–93.
Chakhoyan, A., Yao, J., Leu, K., et al., 2019. Validation of vessel size imaging (VSI) in high-grade human gliomas using magnetic resonance imaging, image-guided biopsies, and quantitative immunohistochemistry. Sci. Reports 9 (1), 2846.
Chappell, M.A., McConnell, F.A.K., Golay, X., et al., 2021. Partial volume correction in arterial spin labeling perfusion MRI: a method to disentangle anatomy from physiology or an analysis step too far? Neuroimage 238, 118236.
Coquery, N., Pannetier, N., Farion, R., et al., 2012. Distribution and radiosensitizing effect of cholesterol-coupled Dbait molecule in rat model of glioblastoma. PLoS. One 7 (7), e40567.
Dennie, J., Mandeville, J.B., Boxerman, J.L., Packard, S.D., Rosen, B.R., Weisskoff, R.M., 1998. NMR imaging of changes in vascular morphology due to tumor angiogenesis. Magnet. Resonance Med. 40 (6), 793–799.
Emblem, K.E., Mouridsen, K., Bjornerud, A., et al., 2013. Vessel architectural imaging identifies cancer patient responders to anti-angiogenic therapy. Nat. Med. 19 (9), 1178–1183.
Farrar, C.T., Kamoun, W.S., Ley, C.D., et al., 2011. Sensitivity of MRI tumor biomarkers to VEGFR inhibitor therapy in an orthotopic mouse glioma model. PLoS. One 6 (3), e17228.
Gil, R., Khabipova, D., Zwiers, M., Hilbert, T., Kober, T., Marques, J.P., 2016. An in vivo study of the orientation-dependent and independent components of transverse relaxation rates in white matter. NMR Biomed. 29 (12), 1780–1790.
Grivas, I., Michaloudi, H., Batzios, C., Chiotelli, M., Papatheodoropoulos, C., Kostopoulos, G., Papadopoulos, G.C., 2003. Vascular network of the rat hippocampus is not homogeneous along the septotemporal axis. Brainresearch 971 (2), 245–249.
Jahng, G.-H., Li, K.-L., Ostergaard, L., Calamante, F., 2014. Perfusion magnetic resonance imaging: a comprehensive update on principles and techniques. Korean Journal of Radiology 15 (5), 554.
Jensen, J., Chandra, R., 2000. MR imaging of microvasculature. Magnet. Resonance Med.: Official J. Int. Soc. Magnet. Resonance Med. 44 (2), 224–230.
Jung, H., Park, B., Lee, C., et al., 2014. Dual MRI T1 and T2 (*) contrast with size-controlled iron oxide nanoparticles. Nanomed.: Nanotechnol., Biol. Med. 10 (8), 1679–1689.
Kim, S.G., Harel, N., Jin, T., Kim, T., Lee, P., Zhao, F, 2013. Cerebral blood volume MRI with intravascular superparamagnetic iron oxide nanoparticles. NMR Biomed. 26 (8), 949–962.
Kiselev, V.G., Posse, S., 1998. Analytical theory of susceptibility induced NMR signal dephasing in a cerebrovascular network. Phys. Rev. Lett. 81 (25), 5696.
Kiselev, V., Posse, S., 1999. Analytical model of susceptibility-induced MR signal dephasing: effect of diffusion in a microvascular network. Magnet. Resonance Med.: Official J. Int. Soc. Magnet. Resonance Med. 41 (3), 499–509.
Kiselev, V.G., Strecker, R., Ziyeh, S., Speck, O., Hennig, J., 2005. Vessel size imaging in humans. Magnet. Resonance Med.: Official J. Int. Soc. Magnet. Resonance Med. 53 (3), 553–563.
Kolinko, Y., Marsalova, L., Proskauer Pena, S., Kralickova, M., Mouton, P.R, 2021. Stereological changes in microvascular parameters in hippocampus of a transgenic rat model of Alzheimer's disease. J. Alzheimer's Dis. 84 (1), 249–260.
Lee, D., Song, Y.K., Park, B., et al., 2018. The robustness of T 2 value as a trabecular structural index at multiple spatial resolutions of 7 Tesla MRI. Magnet. Resonance Med. 80 (5), 1949–1961.
Lee, D., Kang, M., Cho, H., 2020. MRI size assessment of cerebral microvasculature using diffusion-time-dependent stimulated-echo acquisition: A feasibility study in rodent. Neuroimage 215, 116784.
Lemasson, B., Christen, T., Tizon, X., et al., 2011. Assessment of multiparametric MRI in a human glioma model to monitor cytotoxic and anti-angiogenic drug effects. NMR Biomed. 24 (5), 473–482.
Lin, C.-Y., Chang, C., Cheung, W.-M., et al., 2008. Dynamic changes in vascular permeability, cerebral blood volume, vascular density, and size after transient focal cerebral ischemia in rats: evaluation with contrast-enhanced magnetic resonance imaging. J. Cerebral Blood Flow Metabol. 28 (8), 1491–1501.
Lu, J., Dai, G., Egi, Y., et al., 2009. Characterization of cerebrovascular responses to hyperoxia and hypercapnia using MRI in rat. Neuroimage 45 (4), 1126–1134.
Matsuda, H., Ohnishi, T., Asada, T., et al., 2003. Correction for partial-volume effects on brain perfusion SPECT in healthy men. J. Nuclear Med. 44 (8), 1243–1252.
Meloche, R., Vučković, I., Mishra, P.K., Macura, S., 2022. Transverse relaxation in fixed tissue: Influence of temperature and resolution on image contrast in magnetic resonance microscopy. NMR Biomed. 35 (9), e4747.
Moisan, A., Pannetier, N., Grillon, E., et al., 2012. Intracerebral injection of human mesenchymal stem cells impacts cerebral microvasculature after experimental stroke: MRI study. NMR Biomed. 25 (12), 1340–1348.
Oouchi, H., Yamada, K., Sakai, K., et al., 2007. Diffusion anisotropy measurement of brain white matter is affected by voxel size: underestimation occurs in areas with crossing fibers. Am. J. Neuroradiol. 28 (6), 1102–1106.
Packard, S.D., Mandeville, J.B., Ichikawa, T., Ikeda, K., Terada, K., Niloff, S., Chiocca, E. A., Rosen, B.R., Marota, J.J., 2003. Functional response of tumor vasculature to PaCO2: determination of total and microvascular blood volume by MRI. Neoplasia 5 (4), 330–338.
Pankhurst, Q.A., Connolly, J., Jones, S.K., Dobson, J., 2003. Applications of magnetic nanoparticles in biomedicine. J. Phys. D:Appl. Physics 36 (13), R167.
Pannetier, N., Lemasson, B., Christen, T., et al., 2012. Vessel size index measurements in a rat model of glioma: comparison of the dynamic (Gd) and steady-state (iron-oxide) susceptibility contrast MRI approaches. NMR Biomed. 25 (2), 218.
Papp, E.A., Leergaard, T.B., Calabrese, E., Johnson, G.A., Bjaalie, J.G., 2014. Waxholm Space atlas of the Sprague Dawley rat brain. Neuroimage 97, 374–386.
Pathak, A.P., Ward, B.D., Schmainda, K.M., 2008. A novel technique for modeling susceptibility-based contrast mechanisms for arbitrary microvascular geometries: the finite perturber method. Neuroimage 40 (3), 1130–1143.
Quarles, C.C., Schmainda, K.M., 2007. Assessment of the morphological and functional effects of the anti-angiogenic agent SU11657 on 9L gliosarcoma vasculature using dynamic susceptibility contrast MRI. Magnet. Resonance Med.: Official J. Int. Soc. Magnet. Resonance Med. 57 (4), 680–687.
Rossi, C., Sharma, P., Pazahr, S., Alkadhi, H., Nanz, D., Boss, A., 2013. Blood oxygen level–dependent magnetic resonance imaging of the kidneys: influence of spatial resolution on the apparent R2* transverse relaxation rate of renal tissue. Investigat. Radiol. 48 (9), 671–677.
Schlageter, K.E., Molnar, P., Lapin, G.D., Groothuis, D.R., 1999. Microvessel organization and structure in experimental brain tumors: microvessel populations with distinctive structural and functional properties. Microvasc. Res. 58 (3), 312–328.
Serduc, R., Christen, T., Laissue, J., et al., 2008. Brain tumor vessel response to synchrotron microbeam radiation therapy: a short-term in vivo study. Phys. Med. Biol. 53 (13), 3609.
Troprès, I., Lamalle, L., Peoc'h, M., Farion, R., Usson, Y., Décorps, M., Remy, C, 2004. In vivo assessment of tumoral angiogenesis. Magnet. Resonance Med.: Official J. Int. Soc. Magnet. Resonance Med. 51 (3), 533–541.
Troprès, I., Pannetier, N., Grand, S., et al., 2015. Imaging the microvessel caliber and density: principles and applications of microvascular MRI. Magnet. Resonance Med. 73 (1), 325–341.
Tropres, I., Grimault, S., Vaeth, A., et al., 2001. Vessel size imaging. Magnet. Resonance Med.: Official J. Int. Soc. Magnet. Resonance Med. 45 (3), 397–408.
Tropres, I., Lamalle, L., Farion, R., Segebarth, C., Remy, C, 2004. Vessel size imaging using low intravascular contrast agent concentrations. Magnet. Resonance Mater. Phys., Biol. Med. 17 (3), 313–316.
Valable, S., Lemasson, B., Farion, R., et al., 2008. Assessment of blood volume, vessel size, and the expression of angiogenic factors in two rat glioma models: a longitudinal in vivo and ex vivo study. *NMR Biomed.: Int. J. Devoted Develop. Appl. Magnet. Resonance* In vivo 21 (10), 1043–1056.
Weidensteiner, C., Metzger, F., Bohrmann, A.B.B., Kuennecke, B., von Kienlin, M., 2009. Cortical hypoperfusion in the B6. PS2APP mouse model for Alzheimer's disease: comprehensive phenotyping of vascular and tissular parameters by MRI. Magnet. Resonance Med.: Official J. Int. Soc. Magnet. Resonance Med. 62 (1), 35–45.
Xia, Y., 1998. Relaxation anisotropy in cartilage by NMR microscopy (μMRI) at 14-μm resolution. Magn. Reson. Med. 39 (6), 941–949.
Yablonskiy, D.A., Haacke, E.M., 1994. Theory of NMR signal behavior in magnetically inhomogeneous tissues: the static dephasing regime. Magnet. Resonance Med. 32 (6), 749–763.